A metal–organic framework-derived bifunctional oxygen electrocatalyst

Xia, Bao Yu; Yan, Ya; Li, Nan; Wu, Hao Bin; Lou, Xiong Wen (David); Wang, Xin

2016

Xia, B. Y., Yan, Y., Li, N., Wu, H. B., Lou, X. W., & Wang, X. (2016). A metal–organic framework-derived bifunctional oxygen electrocatalyst. Nature Energy, 1, 15006-.

https://hdl.handle.net/10356/84539

https://doi.org/10.1038/nenergy.2015.6

A metal-organic-framework-derived bi-functional oxygen electrocatalyst

Bao Yu Xia[1], Ya Yan[1], Nan Li[1], Hao Bin Wu[1], Xiong Wen (David) Lou[1] & Xin Wang[1]

School of Chemical and Biomedical Engineering, Nanyang Technological University, 62 Nanyang Drive, Singapore 637459, Singapore

Correspondence and requests for materials should be addressed to
X. W. L. (xwlou@ntu.edu.sg) or X. W. (WangXin@ntu.edu.sg).

Oxygen electrocatalysis is of great importance for many energy storage and conversion technologies including fuel cells, metal-air batteries and water electrolysis. Replacing noble metal-based electrocatalysts with highly efficient and inexpensive non-noble metal based oxygen electrocatalysts is critical for the practical applications of these technologies. Here we report a general approach for the synthesis of hollow frameworks of nitrogen-doped carbon nanotubes derived from metal-organic frameworks, which exhibit higher electrocatalytic activity and stability for oxygen reduction and evolution than commercial Pt/C electrocatalysts. The remarkable electrochemical properties are mainly attributed to the synergistic effect from chemical compositions and the robust hollow structure composed of interconnected crystalline nitrogen-doped carbon nanotubes. The presented strategy for controlled design and synthesis of metal-organic framework-derived functional nanomaterials offers prospects in developing highly active electrocatalysts in electrochemical energy devices.

Oxygen electrochemistry involves oxygen reduction (ORR) and evolution (OER) reactions, which are the two most important reactions for electrochemical energy storage and conversion technologies including fuel cells, metal-air batteries and water electrolysis.[1,2] A highly active and stable electrocatalyst for ORR and OER is the key for these electrochemical applications.[3] Noble metals are normally good electrocatalysts for these applications. For example, platinum (Pt)-based nanocomposites are the most efficient commercial electrocatalysts for ORR, while precious ruthenium (Ru) and iridium (Ir) based nanocomposites are commonly used in the OER process.[4] However, the poor stability, scarcity and high cost of these noble metal-based oxygen electrocatalysts are the major barriers for the large-scale implementation of these technologies.[5,6] Thus, it is urgent to develop highly efficient and low-cost durable alternatives ideally with the bi-functional capability for the reversible ORR and OER.[7] In the past decade, a wide range of alternative materials, including nanocarbons,[8] metal oxides,[9] carbides/nitrides and their composites,[10-13] have been found electroactive towards the oxygen electrochemical processes.[14-16] Among them, nanocarbons are demonstrated with the promising catalytic activity and stability,[4,8,17] and the catalytic properties could be further enhanced by the introduction of heteroatoms including N, S, and B etc.[18] through the modification of electronic and geometric structures.[19] In particular, various N-doped graphitic nanocarbons including carbon nanotubes (CNTs), graphene, mesoporous carbons and their nanocomposites have been reported as possible replacements for Pt catalysts.[20-22] The enhanced performance is believed to be related to the modified electronic structure and carbon defects induced by the foreign heteroatoms.[23] However, few reports of nanocarbons have so far shown excellent activity and durability comparable to that of Pt/C catalysts.[24]

Recently, metal-organic frameworks (MOFs) have emerged as a new platform for synthesis of new nanocarbon composites.[25-27] As a subclass of MOFs, zeolitic imidazolate frameworks (ZIFs) are excellent precursors for nanocarbon electrocatalysts in view of the existence of abundant carbon and nitrogen species.[28-30] The nitrogen species would form chemical bonds with metal nanoparticles and serve as the heteroatoms in the formed N-doped carbon materials.[31] Such N-doped nanocarbons may be promising electrocatalysts for ORR and OER.[32] Unfortunately, the MOFs-derived nanocomposites are mostly microporous and of poor graphitic degree,[33] which are considered unfavourable for ion and electron transport. Although a number of MOFs-derived nanocarbons/metal oxides have been investigated as

electrocatalysts,[34-36] most of them exhibit unsatisfactory electrochemical activity. Moreover, it is rarely reported to use MOFs as the single precursor for preparation of N-doped CNTs (NCNT) structures so far.[37,38] Yang et al. demonstrated the synthesis of NCNTs through the pyrolysis of Zn-Fe-ZIFs. In their synthesis, dicyandiamide (DCDA) is introduced as the inducer of graphitic structure and extra N source, and the formed NCNTs do not retain any secondary microstructure.[39]

Herein, we report the direct synthesis of N-doped carbon nanotube frameworks (NCNTFs) derived from MOFs as an active and stable bi-functional electrocatalyst for the ORR and the OER. The as-prepared hollow structures retain the well-defined morphology of the initial ZIF-67 particles with hierarchical shells of interconnected crystalline N-doped CNTs. With many advantageous features in composition, structure and optimum graphitic degree and N-doping level, the resultant NCNTFs show enhanced activity and durability as well as methanol tolerance when benchmarked with a commercial Pt/C electrocatalyst under the same testing conditions. Their electrocatalytic activities in terms of onset and half-wave potentials for the ORR compare favourably with various nanocarbons reported so far. It is also important to point out that the MOFs material is the single precursor for the formation of NCNTs structures in this work.

Electrocatalyst preparation and characterization

The NCNTFs material is synthesized by a simple thermal treatment of purple ZIF-67 particles (Supplementary Fig. 1) containing abundant C, Co and N atoms at 700 ^{o}C in Ar/H_2 atmosphere followed by acid treatment of the resulting material with 0.5 M H_2SO_4 for 6 h to remove the accessible Co nanoparticles. Fig. 1a shows a typical field-emission scanning electron microscopy (FESEM) image of the as-obtained NCNTFs. The size and polyhedral shape of the ZIF-67 nanoparticles are retained well after thermal treatment, while the surface of the particles becomes much rougher (Fig. 1b). Many tiny CNTs can be observed on the rough surface. Moreover, some particles show open voids, indicating the formation of hollow structures. The hierarchical shell, with thickness of about 200 nm, is composed of interconnected CNTs (Fig. 1c). The microstructure is further investigated by transmission electron microscopy (TEM; Supplementary Fig. 2). Fig. 1d confirms the hollow structure with a shell composed of CNTs with several hundred nanometres in length. TEM image also reveals the presence of Co nanoparticles encapsulated by a

few-layered carbon shell, especially at the tip of CNTs (Fig. 1e). These carbon encased Co nanoparticles are inaccessible to reactants as they remain completely encapsulated within the graphitic carbon shell even after acid leaching. Furthermore, high-resolution (HR)TEM image reveals that these thick multi-walled CNTs are crystalline and the lattice fringes with an inter-planar distance of ~0.36 nm correspond to the C(002) plane (Fig. 1f). It is interesting to observe that the graphitic layers in the CNT walls are not perfectly parallel to the axis direction of the CNTs, thus abundant edges rather than the basal plane are exposed on the surface of the CNTs (Fig.1e, 1f), which would be beneficial to the enhanced electrocatalytic properties.

The crystalline nature of the carbon material in the frameworks is further confirmed by powder X-ray diffraction (XRD) in Fig. 2a. The peak at about 26.2^{o} corresponds to the C(002) plane, and the other peak at about 44.3^{o} is attributed to metallic Co. Raman spectra of the products also reveal the characteristic G and D bands of carbon , which are related to the graphitic sp^2-carbon and disordered or defect carbon respectively (Supplementary Fig. 3a,b). The chemical composition and the effect of N doping are investigated by X-ray photoelectron spectroscopy (XPS; Supplementary Fig. 3c). The high-resolution C1s spectrum can be deconvoluted into two bands, corresponding to C-C at ~284.5 eV and C=N at ~285.6 eV (Fig. 2b). The high-resolution N1s spectrum reveals the presence of two types of nitrogen species, pyridinic N at ~398.5 eV and pyrrolic N at ~ 400.8 eV (Fig. 2c and Supplementary Fig. 4). The atomic percentage of N dopant is about 2.4% for the NCNTFs obtained at 700 ^{o}C (Supplementary Fig. 3d). The Co 2p spectrum exhibits two prominent bands at 779.2 eV and 794.7 eV, readily assigned to Co $2p_{3/2}$ and Co $2p_{1/2}$ respectively (Supplementary Fig. 5a). Based on thermogravimetric analysis (TGA), the Co atomic fraction is found to be about 3.1% (Supplementary Fig. 5b), which is larger than 1.14 % by XPS analysis, probably due to the limited sampling depth of XPS. A slight increase in the content of the surface Co species with higher pyrolysis temperature is observed from the XPS results (Supplementary Fig. 3d), which may be explained by the enhanced graphitic degree with the increase in pyrolysis temperature. N_2 sorption isotherms of NCNTFs can be identified as type-IV isotherms with a pronounced hysteresis loop, suggesting the existence of mesoporous structure (Fig. 2d and Supplementary Fig. 6). Moreover, the NCNTFs sample shows a relatively broad mesopore distribution with an average pore size of ~7.8 nm (inset of Fig. 2d). The specific

surface area estimated by the Brunauer-Emmett-Teller (BET) method and the total volume are 513 m^2 g^{-1} and 1.16 cm^3 g^{-1}, respectively (Supplementary Fig. 6d).

During the heat treatment, the H_2 atmosphere plays a critical role on the formation of hollow structured hierarchical CNTs frameworks. Metallic Co nanoparticles are quickly formed in the presence of H_2 atmosphere, followed by the catalytic growth of NCNTs and eventually formation of NCNTFs. In this process, ZIF-67 particles serve not only as the C and N source for growth of N-doped CNTs with the assistance of metallic Co catalysts but also as the self-template for the framework morphology.[40] The fast pyrolysis of imidazolate and gradual consumption of C by growing CNTs take place simultaneously leading to the formation of inner hollow structure.[41] It is worth noting that the hollow structure is formed during the heat treatment process, as evident from the observation of samples without acid leaching treatment (Supplementary Fig. 7 and 8). Only polyhedron-shaped particles are obtained in the absence of H_2 even for the pyrolysis temperature up to 900 ^oC (Fig. 3a, 3b), which is similar to previous reports about ZIFs-derived nanocarbon composites (Supplementary Fig. 9 and 10).[29,34,42] To better understand the evolution of NCNTFs, ZIF-67 particles pyrolyzed in the presence of H_2 at different temperatures are further investigated. At a lower temperature of 600 ^oC, the surface of framework nanoparticles shows some openings and numerous short CNTs clusters (Supplementary Fig. 11), which is mainly attributed to the incomplete pyrolysis of ZIFs and insufficient growth of CNTs (Fig. 3c). With the increase of temperature to 900 ^oC (Fig. 3d), more complete pyrolysis allows the formation of longer CNTs with higher density while the surface of particles becomes much rougher (Supplementary Fig. 12-15). It is therefore remarkably different from all previous reports of formation of microporous nanocarbon and/or metal oxide nanocomposites by direct carbonization of MOFs under inert atmosphere. Similar carbon nanotube frameworks can also be obtained when the present pyrolysis method is applied on other ZIF particles (Fig. 4). Therefore, the current approach offers a versatile new strategy for controlled design and synthesis of MOFs-derived nanomaterials considering the large variety of MOFs particles available.

Electrocatalyst activity and stability

The electrocatalytic activity of the as-prepared NCNTFs is first investigated by cyclic voltammetry (CV). As shown in Fig. 5a, no obvious redox peak is observed for NCNTFs in N_2-saturated KOH solution. In contrast, when the solution is saturated with O_2, a well-defined cathodic peak is clearly observed at ~0.87 V indicating the excellent electrocatalytic activity for ORR. Linear sweep voltammetry (LSV) measurements at different rotation rates for all NCNTFs samples prepared at different temperatures are further conducted with a rotating disk electrode (RDE) setup (Fig. 5b and Supplementary Fig. 16). While all NCNTFs samples exhibit prominent catalytic activity for ORR, the more positive onset potential of the NCNTFs sample obtained at 700 ^{o}C suggests its superior activity (Supplementary Fig. 17a). The kinetic parameters are analysed by the Koutecky-Levich (K-L) equation (Supplementary Note 1), and the linearity of the K-L plots indicates the first-order reaction kinetics with regard to the concentration of dissolved oxygen and similar electron transfer numbers (*n*) at various potentials (Fig. 5c). The value of *n* is calculated to be in the range 3.97-3.99 for the potential range 0.3 V to 0.7 V, which is close to the theoretical value of 4.00 for Pt/C, indicating a complete 4e ORR pathway. The NCNTFs sample is benchmarked with a commercial Pt/C electrocatalyst for ORR (Supplementary Fig. 17b), which also exhibits a nearly 4e ORR pathway (*n*=3.96, Supplementary Fig. 17c). Remarkably, the NCNTFs sample obtained at 700 ^{o}C exhibits higher ORR activity than the commercial Pt/C electrocatalyst in terms of half-wave potential ($E_{1/2}$) (0.87 V vs. 0.84 V in Fig. 5d). The better ORR activity of the NCNTFs is further confirmed by a smaller Tafel slope (~64 mV dec^{-1} vs. ~77 mV dec^{-1} for Pt/C, Supplementary Fig. 17d). Importantly, the present NCNTFs material also exhibits attractive electrocatalytic activity in terms of the onset and half-wave potentials for ORR among numerous nanocarbons reported so far and MOFs-derived electrocatalysts (Supplementary Table 1, Supplementary Fig. 18 and 19). To monitor the hydrogen peroxide yield (% H_2O_2), rotating ring-disk electrode (RRDE) measurements are carried out and the results are presented in Fig. 5e and 5f. In the potential range investigated, the yield of H_2O_2 is below 1.6% and the calculated electron transfer number ranges from 3.97 to 4.00 (Supplementary Fig. 20), which is consistent with the results obtained from the K-L plots based on RDE results (Fig. 5c). Furthermore, unlike most non-Pt electrocatalysts, the NCNTFs catalyst also displays high ORR activity in 0.5 M H_2SO_4 solution with an onset potential of ~0.85 V. The

linearity of K-L plots and the calculated electron transfer number of ~3.88 in acidic solution also confirm the excellent activity of the NCNTFs catalyst (Supplementary Fig. 21).

The possible fuel crossover effect and durability are important issues for cathodic catalysts in fuel cells. The fuel crossover effect is examined by cycling the NCNTFs and Pt/C catalysts from 0.2 to 1.2 V in both O_2-saturated 0.1 M KOH and O_2-saturated 0.1 M KOH + 0.5 M methanol solutions. No obvious change in the current density on the NCNTFs catalyst is observed with or without the presence of 0.5 M methanol in the solution (Fig. 6a). While for Pt/C, the cathodic ORR peak vanishes and one pair of anodic peaks at 1.09 and 1.03 V appears for the oxidation of methanol (Supplementary Fig. 22). Additionally, the chronoamperametric response at 0.6 V is measured on both Pt/C and NCNTFs catalysts in O_2-saturated 0.1 M KOH solution with a rotation rate of 1600 rpm. A significant decrease in the current density is observed upon the addition of 50 mL of methanol in the case of Pt/C catalyst, while the current density is not sensitive to the addition of methanol for the NCNTFs catalyst (Fig. 6b). The above results indicate that the NCNTFs catalyst has excellent tolerance to methanol crossover. Furthermore, the short-term stability of NCNTFs and Pt/C catalysts are investigated at 0.6 V for 100000 s in O_2-saturated 0.1 M KOH solution with a rotation rate of 1600 rpm (Fig. 6c). During the period, about 96% of the original current density is retained for the NCNTFs electrode, while the Pt/C electrode shows a much higher current loss of ~29%, suggesting the superior stability of the former. The NCNTFs catalyst is further subject to a CV test from 0.2 V to 1.2 V for 5000 cycles. LSV curves of NCNTFs show negligible performance loss after the test (Supplementary Fig. 23a). There is only a negative shift of ~7 mV in the $E_{1/2}$ value at 1600 rpm (Fig. 6d) and the Tafel slope remains virtually unchanged (Supplementary Fig. 23b). The excellent stability of NCNTFs is ascribed to the robust framework structure composed of interconnected crystalline NCNTs which retains its original morphology and structure after the cycling test, as confirmed by TEM analysis (Supplementary Fig. 23c, d).

The oxygen evolution activities of the NCNTFs and Pt/C catalysts are also investigated and compared. As shown in Fig. 7a, the NCNTFs catalyst gives a current density of 10 mA cm^{-2} (based on geometric electrode area) at a potential of 1.60 V vs. Reversible Hydrogen Electrode (RHE), which compares favourably to other reported nanocarbon-based catalysts (Supplementary Table 2) and IrO_2/C catalyst (10

mA cm^{-2}, 1.60 V).[22] For the Pt/C catalyst, the potential required to generate a current density of 10 mA cm^{-2} is about 1.78 V, roughly ~180 mV higher than that of NCNTFs. The current density is also normalized by the specific surface area and electrochemical active surface area and the results show similar trend (Supplementary Fig. 24 and 25). The much smaller Tafel slope of NCNTFs further confirms the superior electrochemical OER performance compared to that of Pt/C catalyst (93 vs. 118 mV dec^{-1} in Fig. 7b). The OER activity of different NCNTFs catalysts prepared at various temperatures is given in Fig. 7c and further compared with other MOFs-derived materials (Supplementary Fig. 26). Again the sample obtained at 700 ^{o}C exhibits the best OER activity as it requires the smallest overpotential to achieve the same current density (e.g., 10 mA cm^{-2}). The stability test results demonstrate that the NCNTFs catalyst is very stable for OER (Fig.7d and Supplementary Fig. 27), while Pt/C exhibits a continuous current loss during the stability test. These results suggest that the NCNTFs material is an efficient bi-functional electrocatalyst for reversible oxygen reduction and evolution (Supplementary Table 1 and 2).

Mechanistic study on electrocatalyst activity

The superior electrocatalytic activities of NCNTFs may mainly be attributed to the chemical composition and structure of formed N-doped CNTs as well as the overall framework structure. In the synthesis, the pyrolysis temperature is clearly a critical factor here. In general, as the pyrolysis temperature is increased from 700 to 1000 ^{o}C, the electrocatalytic activity of resultant NCNTFs decreases as seen from the negative shift of $E_{1/2}$ and deceased current density of ORR (Supplementary Fig. 16a). This may be related to the lower defect density generated as a result of the higher pyrolysis temperature (Supplementary Fig. 2b). These defect sites are normally believed more active than basal planes (Fig. 1e, f). Moreover, the N-doping level also decreases with the increase of pyrolysis temperature due to the instability of N atoms at high temperature, as determined by XPS (Supplementary Fig. 2c, d and 3). The N doping not only induces the electronic interaction with nearby carbon/metal atoms to provide catalytically active sites but also produces structural defects in CNTs to form the O_2 adsorption sites.[43,44] However, NCNTFs obtained at 600 ^{o}C have the highest N-doping content and defect density but exhibit the lowest activity, which might be explained by the incomplete pyrolysis of ZIFs.[45] Moreover, the residual metallic Co nanoparticles encapsulated by carbon shells are also believed to play an important role for the excellent electrocatalytic

activity.[46] It has been previously reported that nanocarbon electrocatalysts have enhanced activity in the presence of metallic nanoparticles by electronic interaction between metal nanoparticles and CNTs.[23,47,48] Furthermore, the high surface area and three-dimensional (3D) hierarchical porous hollow structure are also beneficial for the enhanced mass transport during the electrochemical reaction.[49,50] The robust framework structure consisting of interconnected NCNTs is also very critical for the enhanced electrocatalytic activity and stability because of the excellent conductivity and remarkable corrosion resistance in harsh operation environment.

Conclusions

In summary, starting with ZIF-67 particles as the single precursor, we synthesize a hollow framework constructed from interconnected crystalline NCNTs as an efficient and stable bi-functional electrocatalyst for ORR and OER. During the pyrolysis synthesis, ZIF-67 particles not only provide the C and N source for growth of NCNTs catalysed by the *in-situ* formed metallic Co nanoparticles but also serve as the template for formation of the hollow framework. The as-prepared NCNTFs exhibit remarkable electrocatalytic activity and stability, and even outperform a commercial Pt/C electrocatalyst as a bi-functional electrocatalyst. The exceptional electrocatalytic activity might be mainly attributed to the chemical composition and structure of formed crystalline NCNTs as well as their robust overall framework structure. The facile strategy demonstrated here can be applied for the preparation of many other MOFs-derived functional nanomaterials and opens up a new avenue for developing highly active MOFs-derived electrocatalysts for different electrochemical energy technologies.

Methods

Synthesis of ZIF-67 particles. In a typical synthesis, 2-memthylimizdazole (1.97 g) is dissolved in the mixed solution of 20 mL of methanol and 20 mL of ethanol. $Co(NO_3)_2 \cdot 6H_2O$ (1.746 g) is dissolved in another mixed solution of 20 mL of methanol and 20 mL of ethanol. The above two solutions are then mixed under continuous stirring for 10 s, and the final solution is kept for 20 h at room temperature. The purple precipitate is collected by centrifugation, washed by ethanol several times and dried at 80 ^{o}C. Other ZIF

particles are also obtained using the same method except the use of different molar concentrations of $Co(NO_3)_2 \cdot 6H_2O$ and 2-memthylimizdazole. All chemicals are used as received.

Synthesis of hollow NCNTFs. The ZIF-67 particles are dispersed in a ceramic boat and heated to 350 ^oC and maintained for 1.5 h in a tube furnace. The temperature in furnace is further raised to a set temperature (600, 700, 800, 900, and 1000 ^oC) with a ramp rate of 2 $^oC\ min^{-1}$ and kept at the temperature for 3.5 h. After that, the furnace is cooled down to room temperature naturally. During the pyrolysis process, the furnace is under Ar/H_2 flow (90 %/10% in volume ratio). The as-prepared black powder products are treated in 0.5 M H_2SO_4 solution for 6 h. The resulting samples are collected by centrifugation, repeatedly washed with DI water and dried at 80 ^oC.

Materials characterizations. The morphologies and structures are characterized by field-emission scanning electron microscopy (FESEM; JEOL, JSM-6701F, 5 kV) and transmission electron microscopy (TEM; JEOL, JEM-2010, 200 kV). Powder X-ray diffraction (XRD) patterns are recorded using a Bruker diffractometer with Cu Kα radiation (D8 Advance X-ray diffractometer, Cu Kα, λ = 1.5406 Å, 40 kV and 40 mA) to study the crystallographic information. The N_2 sorption isotherms are collected using a Quantachrome Instruments Autosorb AS-6B at liquid-nitrogen temperature. Raman spectra are collected using a Renishaw system 1000 micro-Raman spectroscope (Renishaw, UK). The surface properties of the samples are analysed by X-ray photoelectron spectroscopy (XPS; VG ESCALAB MKII instrument) with a Mg Kα X-ray source. Before the analysis, all the samples are dried under vacuum at 80 ^oC. Thermogravimetric analysis (TGA, Perkin Pyris Diamond) is performed under air flow (200 mL min^{-1}) with a temperature ramp of 10 $^oC\ min^{-1}$.

Electrochemical measurements. All electrocatalytic measurements are carried out in a three-electrode cell using a rotating disk electrode (RDE, PINE Research Instrumentation) with an Autolab bipotentiostat (Model PGSTAT-72637) workstation at ambient temperature. A platinum foil and Ag/AgCl (3.0 M KCl) are used as the counter and reference electrodes, respectively. All potentials in this study refer to RHE, $E_{(RHE)} = E_{(Ag/AgCl)} + 0.059 \times pH + 0.210$. A RDE with glassy carbon (GC) disk electrode (5 mm in diameter) and a rotating ring-disk electrode (PINE AFE6R2GCPT) with a Pt ring (6.5 mm inner diameter and 8.5 mm outer diameter) and a GC disk (5.5 mm diameter) are used as the substrate for the working electrodes. Before use,

the GC electrodes in RDE/RRDE are polished using aqueous alumina suspension on felt polishing pads. The catalyst suspension is prepared by dispersing 5 mg of catalyst in 1 mL of solution containing 0.98 mL of ethanol and 20 μL of 0.5 wt% Nafion solution followed by ultrasonication for 30 min. Then a certain volume of catalyst suspension is pipetted onto the GC surface to give a 0.2 mg cm^{-2} loading for all samples including commercial Pt/C (40 wt%, Johnson Matthey). Before tests, N_2/O_2 flow is used through the electrolyte in the cell to achieve the N_2/O_2-saturated solution. The cyclic voltammetry (CV) profiles are obtained in N_2- or O_2-saturated 0.1 M KOH solution with a scan rate of 20 mV s^{-1}. RDE/RRDE tests for ORR are measured in O_2-saturated 0.1 M KOH solution at different rotation rates with a scan rate of 10 mV s^{-1}. For fuel crossover effect tests, chronoamperometric response at 0.6 V is recorded by RDE tests with a rotation rate of 1600 rpm and followed by the introduction of 50 mL of methanol into 150 mL of 0.1 M KOH solution. Linear sweep voltammograms for OER are obtained using a RDE (1600 rpm), corrected by *iR*-compensation in 1 M KOH solution at a scan rate of 5 mV s^{-1}. Solution resistance is determined by the high frequency intercept from the Nyquist plot obtained by electrochemical impedance spectroscopy (EIS) technique. The ring collection efficiency in RRDE experiment is determined at 0.35 in a 10 mM $K_3[Fe(CN)_6]$ and 0.1 M KNO_3 solution. For detection of peroxide species formed at the disc electrode, the potential of the Pt ring electrode in RRDE measurements is set at 1.5 V.

References

1 Suntivich, J. *et al.* Design principles for oxygen-reduction activity on perovskite oxide catalysts for fuel cells and metal–air batteries. *Nat. Chem.* **3**, 546-550 (2011).

2 Bruce, P. G., Freunberger, S. A., Hardwick, L. J. & Tarascon, J.-M. Li-O_2 and Li-S batteries with high energy storage. *Nat. Mater.* **11**, 19-29 (2012).

3 Debe, M. K. Electrocatalyst approaches and challenges for automotive fuel cells. *Nature* **486**, 43-51 (2012).

4 Wu, G. & Zelenay, P. Nanostructured nonprecious metal catalysts for oxygen reduction reaction. *Acc. Chem. Res.* **46**, 1878-1889 (2013).

5 Borup, R. *et al.* Scientific aspects of polymer electrolyte fuel cell durability and degradation. *Chem. Rev.* **107**, 3904-3951 (2007).

6 Meier, J. C. *et al.* Stability investigations of electrocatalysts on the nanoscale. *Energy Environ. Sci.* **5**, 9319-9330 (2012).

7 Chen, Z., Higgins, D., Yu, A., Zhang, L. & Zhang, J. A review on non-precious metal electrocatalysts for PEM fuel cells. *Energy Environ. Sci.* **4**, 3167-3192 (2011).

8 Li, Q., Cao, R., Cho, J. & Wu, G. Nanocarbon electrocatalysts for oxygen reduction in alkaline media for advanced energy conversion and storage. *Adv. Energy Mater.* **4**, 1301415 (2014).

9 Liang, Y. *et al.* Co_3O_4 nanocrystals on graphene as a synergistic catalyst for oxygen reduction reaction. *Nat. Mater.* **10**, 780-786 (2011).

10 Yang, S., Feng, X., Wang, X. & Müllen, K. Graphene-based carbon nitride nanosheets as efficient metal-free electrocatalysts for oxygen reduction reactions. *Angew. Chem. Int. Ed.* **50**, 5339-5343 (2011).

11 Zheng, Y. *et al.* Nanoporous graphitic-C_3N_4@carbon metal-free electrocatalysts for highly efficient oxygen reduction. *J. Am. Chem. Soc.* **133**, 20116-20119 (2011).

12 Liang, Y., Li, Y., Wang, H. & Dai, H. Strongly coupled inorganic/nanocarbon hybrid materials for advanced electrocatalysis. *J. Am. Chem. Soc.* **135**, 2013-2036 (2013).

13 Ma, T. Y., Dai, S., Jaroniec, M. & Qiao, S. Z. Graphitic carbon nitride nanosheet–carbon nanotube three-dimensional porous composites as high-performance oxygen evolution electrocatalysts. *Angew. Chem. Int. Ed.* **53**, 7281-7285 (2014).

14 Bashyam, R. & Zelenay, P. A class of non-precious metal composite catalysts for fuel cells. *Nature* **443**, 63-66 (2006).

15 Zheng, Y., Liu, J., Liang, J., Jaroniec, M. & Qiao, S. Z. Graphitic carbon nitride materials: controllable synthesis and applications in fuel cells and photocatalysis. *Energy Environ. Sci.* **5**, 6717-6731 (2012).

16 Chen, S., Duan, J., Jaroniec, M. & Qiao, S.Z. Nitrogen and oxygen dual-doped carbon hydrogel film as a substrate-free electrode for highly efficient oxygen evolution reaction. *Adv. Mater.* **26**, 2925-2930 (2014).

17 Proietti, E. *et al.* Iron-based cathode catalyst with enhanced power density in polymer electrolyte membrane fuel cells. *Nat. Commun.* **2**, 416 (2011).

18 Liang, J., Jiao, Y., Jaroniec, M. & Qiao, S. Z. Sulfur and nitrogen dual-doped mesoporous graphene electrocatalyst for oxygen reduction with synergistically enhanced performance. *Angew. Chem. Int. Ed.* **51**, 11496-11500 (2012).

19 Wang, H., Maiyalagan, T. & Wang, X. Review on recent progress in nitrogen-doped graphene: synthesis, characterization, and its potential applications. *ACS Catal.* **2**, 781-794 (2012).

20 Yang, W., Fellinger, T.-P. & Antonietti, M. Efficient metal-free oxygen reduction in alkaline medium on high-surface-area mesoporous nitrogen-doped carbons made from ionic liquids and nucleobases. *J. Am. Chem. Soc.* **133**, 206-209 (2011).

21 Li, Y. *et al.* An oxygen reduction electrocatalyst based on carbon nanotube-graphene complexes. *Nat. Nanotechnol.* **7**, 394-400 (2012).

22 Zhao, Y., Nakamura, R., Kamiya, K., Nakanishi, S. & Hashimoto, K. Nitrogen-doped carbon nanomaterials as non-metal electrocatalysts for water oxidation. *Nat. Commun.* **4**, 2390 (2013).

23 Wu, G., More, K. L., Johnston, C. M. & Zelenay, P. High-performance electrocatalysts for oxygen reduction derived from polyaniline, iron, and cobalt. *Science* **332**, 443-447 (2011).

24 Gong, K., Du, F., Xia, Z., Durstock, M. & Dai, L. Nitrogen-doped carbon nanotube arrays with high electrocatalytic activity for oxygen reduction. *Science* **323**, 760-764 (2009).

25 Yaghi, O. M. *et al.* Reticular synthesis and the design of new materials. *Nature* **423**, 705-714 (2003).

26 Liu, B., Shioyama, H., Akita, T. & Xu, Q. Metal-organic framework as a template for porous carbon synthesis. *J. Am. Chem. Soc.* **130**, 5390-5391 (2008).

27 Wang, C., Liu, D. & Lin, W. Metal–organic frameworks as a tunable platform for designing functional molecular materials. *J. Am. Chem. Soc.* **135**, 13222-13234 (2013).

28 Palaniselvam, T., Biswal, B. P., Banerjee, R. & Kurungot, S. Zeolitic imidazolate framework (ZIF)-derived, hollow-core, nitrogen-doped carbon nanostructures for oxygen-reduction reactions in PEFCs. *Chem. Eur. J.* **19**, 9335-9342 (2013).

29 Zhang, P. *et al.* ZIF-derived in situ nitrogen-doped porous carbons as efficient metal-free electrocatalysts for oxygen reduction reaction. *Energy Environ. Sci.* **7**, 442-450 (2014).

30 Lin, Q. *et al.* New heterometallic zirconium metalloporphyrin frameworks and their teteroatom-activated high-surface-area carbon derivatives. *J. Am. Chem. Soc.* **137**, 2235-2238 (2015).

31 Furukawa, H., Cordova, K. E., O'Keeffe, M. & Yaghi, O. M. The chemistry and applications of metal-organic frameworks. *Science* **341**, 974 (2013).

32 Cao, R. *et al.* Promotion of oxygen reduction by a bio-inspired tethered iron phthalocyanine carbon nanotube-based catalyst. *Nat. Commun.* **4**, 2076 (2013).

33 Jiang, H. L. *et al.* From metal–organic framework to nanoporous carbon: toward a very high surface area and hydrogen uptake. *J. Am. Chem. Soc.* **133**, 11854-11857 (2011).

34 Aijaz, A., Fujiwara, N. & Xu, Q. From metal–organic framework to nitrogen-decorated nanoporous carbons: high CO2 uptake and efficient catalytic oxygen reduction. *J. Am. Chem. Soc.* **136**, 6790-6793 (2014).

35 Wu, Z.-S. *et al.* High-performance electrocatalysts for oxygen reduction derived from cobalt porphyrin-based conjugated mesoporous polymers. *Adv. Mater.* **26**, 1450-1455 (2014).

36 Zhao, D. *et al.* Highly efficient non-precious metal electrocatalysts prepared from one-pot synthesized zeolitic imidazolate frameworks. *Adv. Mater.* **26**, 1093-1097 (2014).

37 Zhao, D. *et al.* Iron imidazolate framework as precursor for electrocatalysts in polymer electrolyte membrane fuel cells. *Chem. Sci.* **3**, 3200-3205 (2012).

38 Zhang, W., Wu, Z.-Y., Jiang, H.-L. & Yu, S.-H. Nanowire-directed templating synthesis of metal–organic framework nanofibers and their derived porous doped carbon nanofibers for enhanced electrocatalysis. *J. Am. Chem. Soc.* **136**, 14385-14388 (2014).

39 Su, P. *et al.* Nitrogen-doped carbon nanotubes derived from Zn-Fe-ZIF nanospheres and their application as efficient oxygen reduction electrocatalysts with in situ generated iron species. *Chem. Sci.* **4**, 2941-2946 (2013).

40 Sun, J.-K. & Xu, Q. Functional materials derived from open framework templates/precursors: synthesis and applications. *Energy Environ. Sci.* **7**, 2071-2100 (2014).

41 Hu, M. *et al.* Direct carbonization of Al-based porous coordination polymer for synthesis of nanoporous carbon. *J. Am. Chem. Soc.* **134**, 2864-2867 (2012).

42 Ma, S., Goenaga, G. A., Call, A. V. & Liu, D.-J. Cobalt imidazolate framework as precursor for oxygen reduction reaction electrocatalysts. *Chem. Eur. J.* **17**, 2063-2067 (2011).

43 Jaouen, F., Serventi, A. M., Lefèvre, M., Dodelet, J.-P. & Bertrand, P. Non-noble electrocatalysts for O_2 reduction: how does heat treatment affect their activity and structure? . *J. Phys. Chem. C* **111**, 5971-5976 (2007).

44 Chung, H. T., Won, J. H. & Zelenay, P. Active and stable carbon nanotube/nanoparticle composite electrocatalyst for oxygen reduction. *Nat. Commun.* **4**, 1922 (2013).

45 Tian, J. *et al.* Optimized synthesis of Fe/N/C cathode catalysts for PEM fuel cells: a matter of iron–ligand coordination strength. *Angew. Chem. Int. Ed.* **52**, 6867-6870 (2013).

46 Wang, L., Ambrosi, A. & Pumera, M. "Metal-free" catalytic oxygen reduction reaction on heteroatom-doped graphene is caused by trace metal impurities. *Angew. Chem. Int. Ed.* **52**, 13818-13821 (2013).

47 Lefèvre, M., Proietti, E., Jaouen, F. & Dodelet, J.-P. Iron-based catalysts with improved oxygen reduction activity in polymer electrolyte fuel cells. *Science* **324**, 71-74 (2009).
48 Deng, D. *et al.* Iron encapsulated within pod-like carbon nanotubes for oxygen reduction reaction. *Angew. Chem. Int. Ed.* **52**, 371-375 (2013).
49 Xiong, W. *et al.* 3-D carbon nanotube structures used as high performance catalyst for oxygen reduction reaction. *J. Am. Chem. Soc.* **132**, 15839-15841 (2010).
50 Liang, H.-W., Zhuang, X., Brüller, S., Feng, X. & Müllen, K. Hierarchically porous carbons with optimized nitrogen doping as highly active electrocatalysts for oxygen reduction. *Nat. Commun.* **5**, 4973 (2014).

Acknowledgements

We acknowledge financial support from the academic research fund AcRF Tier 1 (M4011253, RG 7/14) and Tier 2 (M4020246, ARC10/15) Ministry of Education, Singapore. This project is also funded by the National Research Foundation (NRF), Prime Minister's Office, Singapore under its Campus for Research Excellence and Technological Enterprise (CREATE) programme.

Author contributions

B.Y.X., X.W.L. and X.W. conceived the project and co-wrote the manuscript. B. Y. X carried out the synthesis. B.Y.X., Y.Y., N.L. and H.B.W. conducted the materials characterization and the electrochemical evaluation. B.Y.X. and Y.Y. contributed equally to this work. All authors read and commented on the manuscript.

Additional information

Supplementary Information is available online. Reprints and permission information is available online at http://www.nature.com/reprints. Correspondence and requests for materials should be addressed to X. W. or X. W. L.

Competing financial interests

The authors declare no competing financial interests.

Figures

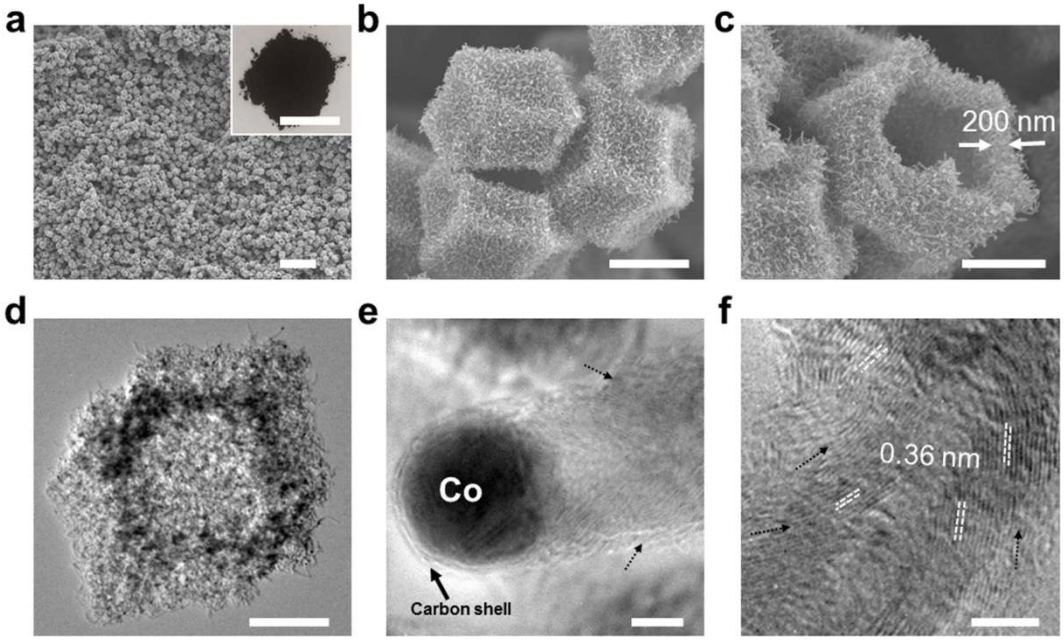

Figure 1 | Morphology and structural characterization of NCNTFs obtained at 700 °C. a,**b**,**c**, FESEM images, **d**, TEM image, **e**,**f**, HRTEM images of NCNTFs obtained at 700 °C in the presence of H_2. In **f**, 0.36 nm refers to the lattice space of carbon (002) plane. Arrows in e and f indicate the direction of graphitic layers. Inset of (**a**) is a digital photo, scale bar is 1 cm. Scale bars: 10 μm (**a**); 1 μm (**b**,**c**); 500 nm (**d**); 5 nm (**e**,**f**).

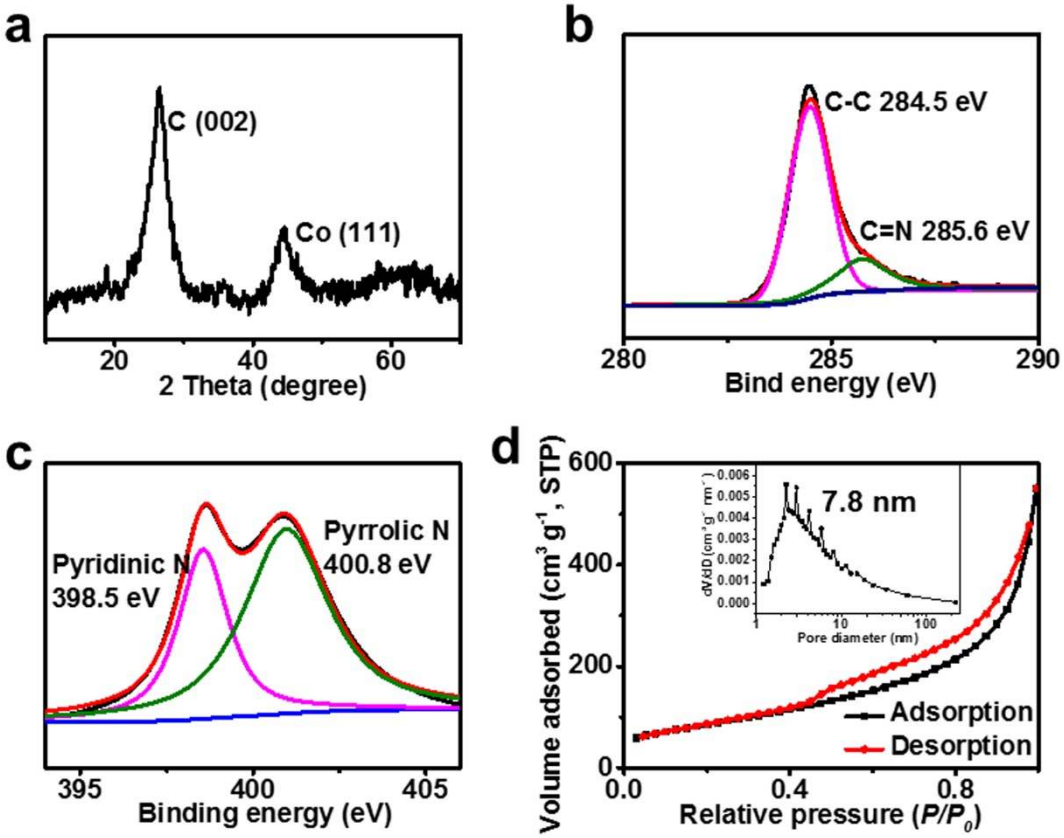

Figure 2 | Compositional and structural information of NCNTFs obtained at 700 °C. a, XRD pattern. **b,c,** High- resolution XPS spectra of C 1s (**b**) and N 1s (**c**). In **b**, the fitted peaks correspond to C-C (284.5 eV) and C=N (285.eV). In **c**, the fitted peaks correspond to pyridinic N (398.5 eV) and pyrrolic N (400.8 eV). **d**, N_2 adsorption-desorption isotherms. Inset of **d** shows the average pore size and pore size distribution derived from the adsorption branch by the Barrett-Joyer-Halenda (BJH) method.

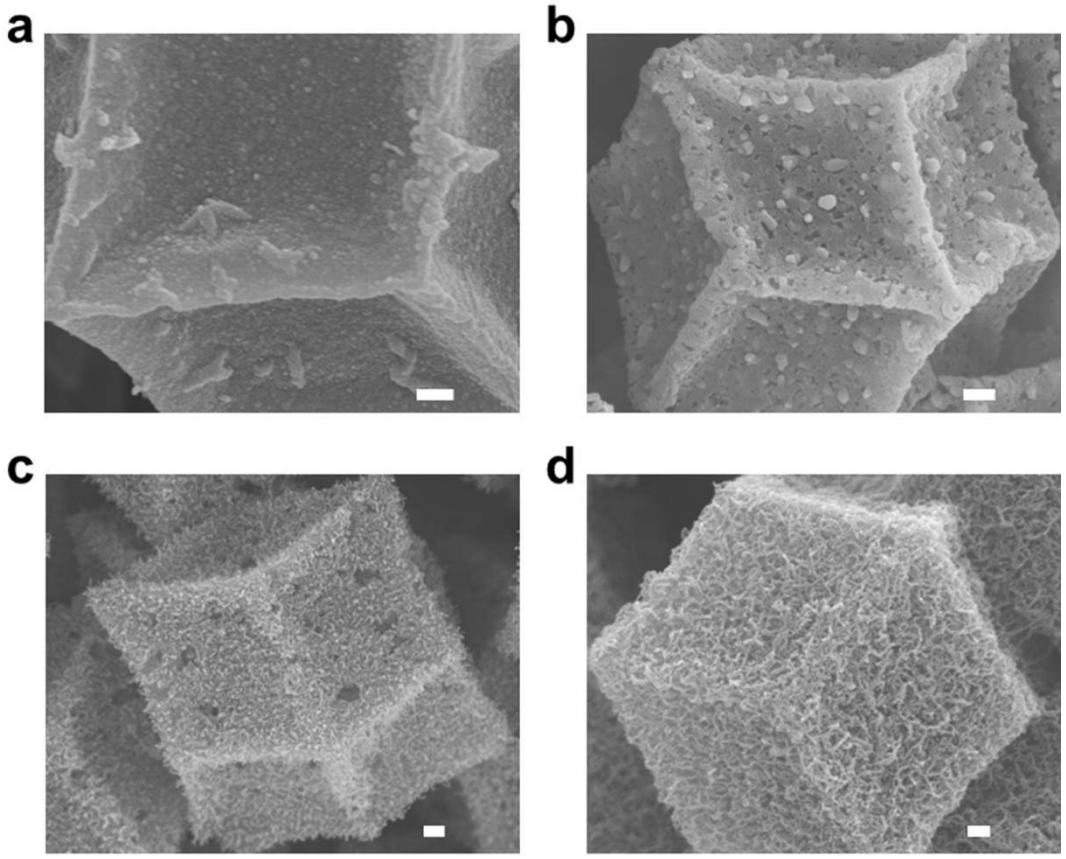

Figure 3 | Morphology and structural characterization of ZIF-derived composites. a,**b**,**c**,**d,** FESEM images of ZIF-67 heat-treated at 600 ^{o}C (**a**) and 900 ^{o}C (**b**) in the absence of H_2; 600 ^{o}C (**c**) and 900 ^{o}C (**d**) in the presence of H_2. All scale bars are 100 nm.

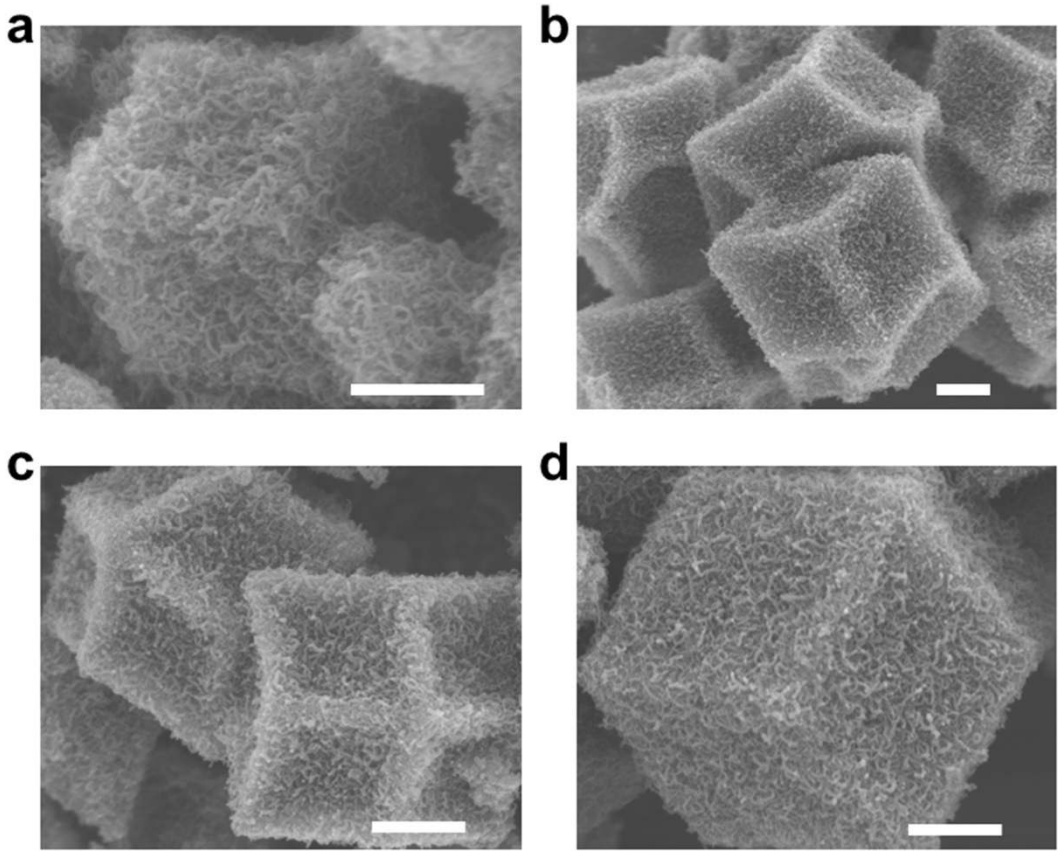

Figure 4 | Morphology and structural characterization of different ZIF-derived NCNTFs. a,**b**, FESEM images of NCNTFs obtained from ZIF-67 with a size of ~500 nm (**a**) and ~1.5 μm (**b**) in the presence of H_2; **c**,**d**, FESEM images of NCNTFs derived from ZIFs with different molar ratios of Co and 2-memthylimizdazole: 1:2 (**c**) and 1:4 (**d**) in the presence of H_2. All scale bars are 500 nm.

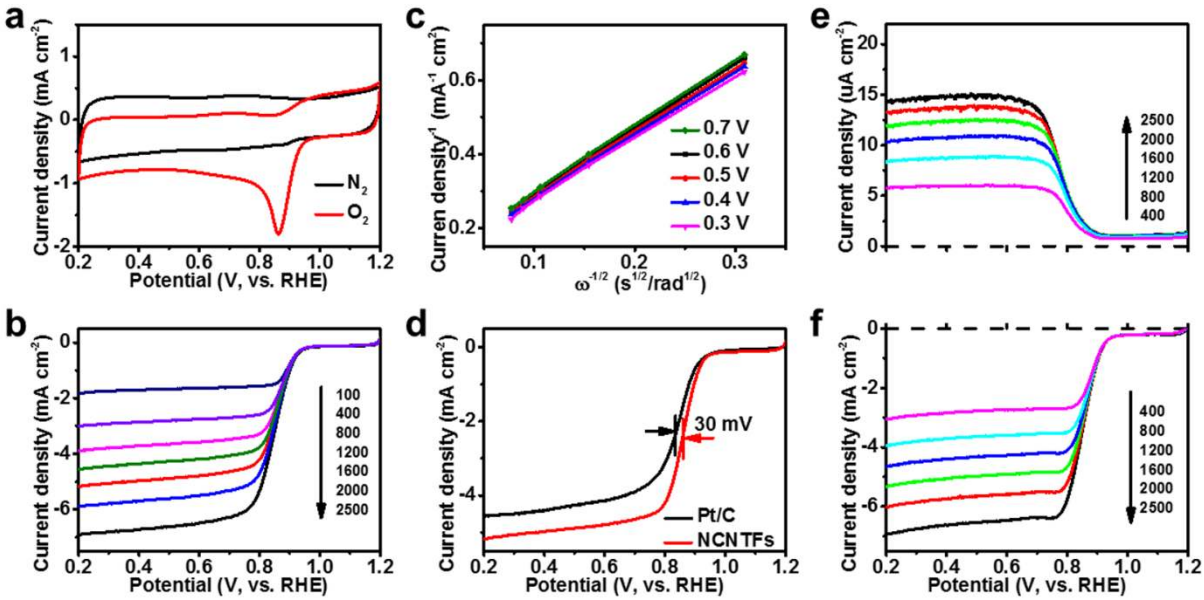

Figure 5 | **Electrochemical oxygen reduction on NCNTFs obtained at 700 °C. a**, CV profiles (black and red curves indicate CV curves recorded in N_2- and O_2-saturated 0.1 M KOH solution, respectively). **b**, LSV curves at different rotation rates (rpm). **c**, K-L plots. **d**, LSV curves of Pt/C and NCNTFs (1600 rpm). **e**,**f**, Ring (**e**) and (**f**) disk current densities in RRDE measurements.

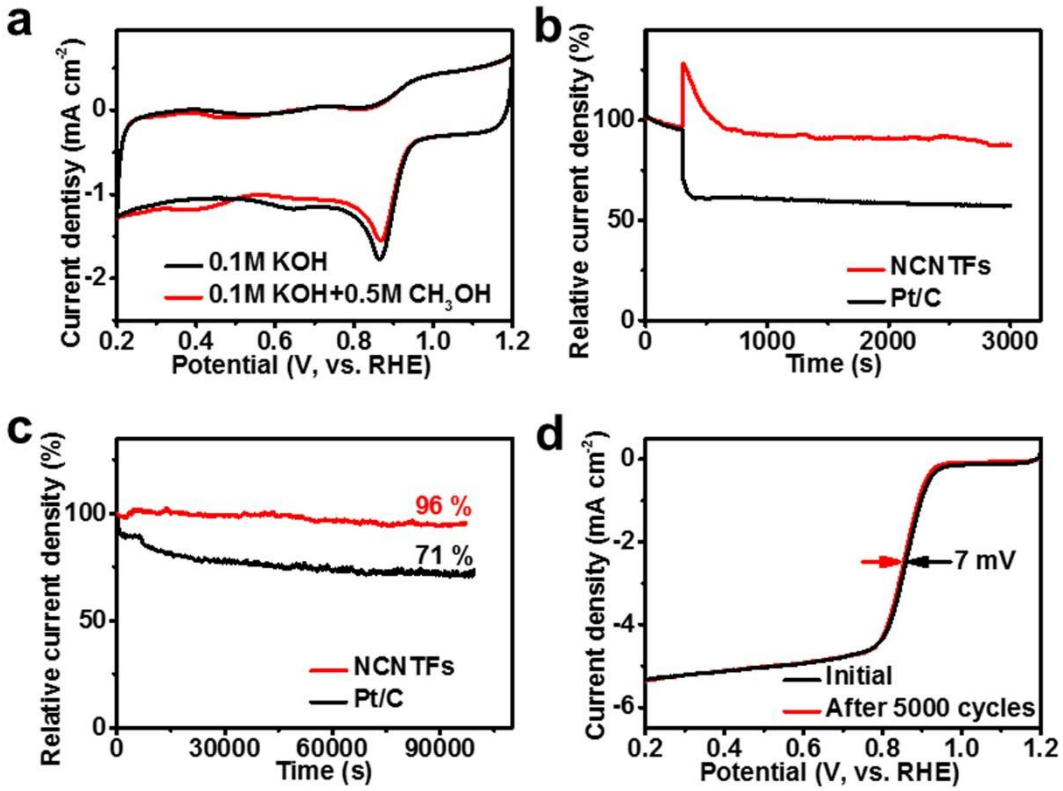

Figure 6 | Electrochemical methanol tolerance and durability of NCNTFs obtained at 700 °C. **a**, CV profiles (black and red curves indicate CV curves recorded in O_2-saturated 0.1 M KOH and O_2-saturated 0.1 M KOH+0.5 M CH_3OH solution, respectively). **b**, Chronoamperometric response at 0.6 V after the introduction of 50 mL of methanol into 150 mL of KOH solution. **c**, Chronoamperometric response at 0.6 V. **d**, ORR polarization curves (1600 rpm) of NCNTFs before and after 5000 cycles.

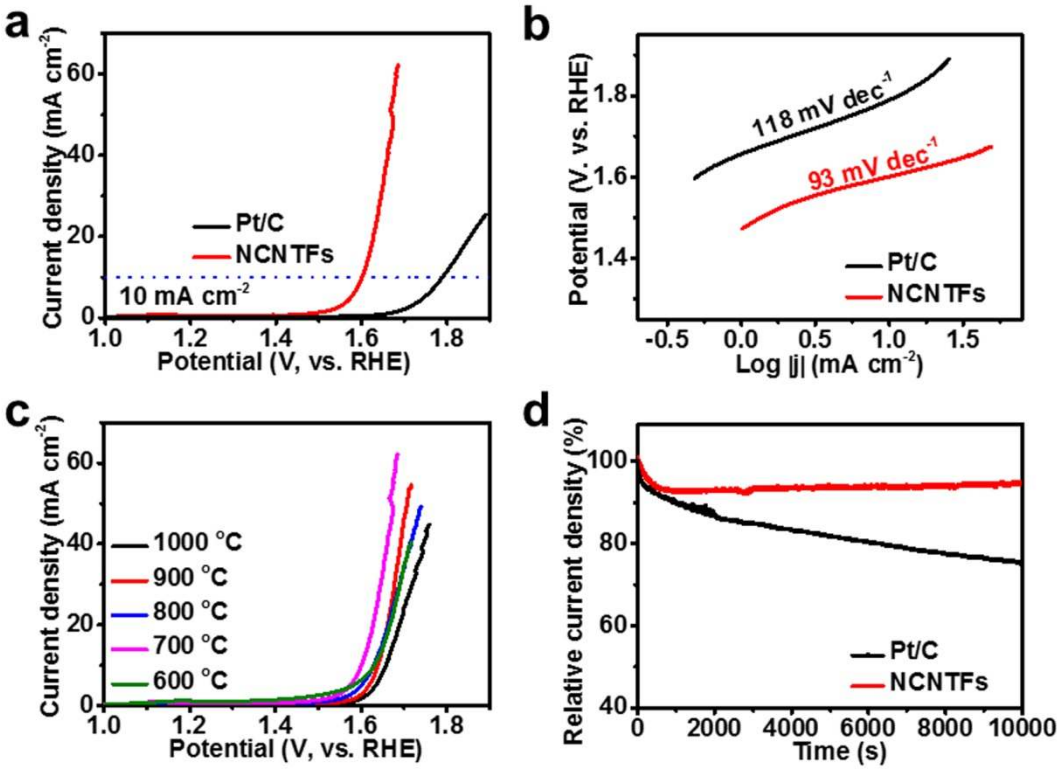

Figure 7 | Electrochemical oxygen evolution on NCNTFs. a, LSV curves of NCNTFs (red) and Pt/C (black) catalysts. **b**, Tafel slopes of NCNTFs (red) and Pt/C (black) catalysts. **c**, LSV curves of NCNTFs catalysts synthesized at different temperatures. **d**, Chronoamperometric response at 1.7 V.